Revealing growth mechanisms of faceted Al_2Cu intermetallic compounds via high-speed Synchrotron X-ray tomography

Song, Zihan; Magdysyuk, Oxana; Sparks, Tay; Chiu, Yu-Lung; Cai, Biao

DOI:
10.1016/j.actamat.2022.117903

Document Version
Publisher's PDF, also known as Version of record

Citation for published version (Harvard):
Song, Z, Magdysyuk, O, Sparks, T, Chiu, Y-L & Cai, B 2022, 'Revealing growth mechanisms of faceted Al_2Cu intermetallic compounds via high-speed Synchrotron X-ray tomography', *Acta Materialia*, vol. 231, 117903. https://doi.org/10.1016/j.actamat.2022.117903

Acta Materialia 231 (2022) 117903

Contents lists available at ScienceDirect

Acta Materialia

journal homepage: www.elsevier.com/locate/actamat

Full length article

Revealing growth mechanisms of faceted Al_2Cu intermetallic compounds via high-speed Synchrotron X-ray tomography

Zihan Song[a], Oxana V. Magdysyuk[b], Tay Sparks[a], Yu-Lung Chiu[a], Biao Cai[a,*]

[a] School of Metallurgy and Materials, University of Birmingham, B15 2TT, UK
[b] Diamond Light Source Ltd, Harwell Science and Innovation Campus, Didcot, OX11 0DE, UK

ARTICLE INFO

Article history:
Received 22 March 2021
Revised 18 January 2022
Accepted 28 March 2022
Available online 30 March 2022

Keywords:
intermetallic
crystal growth
synchrotron x-ray tomography
magnetic field-assisted solidification

ABSTRACT

This study used high-speed synchrotron X-ray tomography to image the growth of Al_2Cu intermetallic compounds in 4D (3D plus time) during solidification of Al-45wt%Cu alloy. Two categories of growth patterns (basic units and dendrites) are identified. Basic units are elongated rods whose cross-section are L, U or hollow-rectangular shapes. The transition from L pattern to U and finally to hollow-rectangular shaped morphology is observed. Faceted dendritic patterns include equiaxed prism and columnar dendrites. Self-repeated layer-by-layer stacking of the basic units (such as L shaped particles) is proposed as a governing mechanism for the growth of Al_2Cu faceted dendrites. The growth orientation and morphologies of these patterns are strongly influenced by solidification conditions (temperature gradients, cooling rates and external magnetic fields). Another finding is that when rotating Al-45wt%Cu during upwards directional solidification, under a transverse magnetic field of 0.5T, highly refined and well aligned Al_2Cu intermetallic compounds are obtained, much finer than those without the imposition of the magnetic field. This is attributed to a rotational stirring flow that modulates and regulates the temperature and solute distribution. The developed experimental findings provide a physical understanding of the formation of faceted intermetallic compounds during solidification.

1. Introduction

Understanding microstructure formation is key in a broad range of solidification processes ranging from casting to welding [1–3]. The morphologies of solidified microstructures were classified into faceted and non-faceted patterns [4]. Growth mechanisms of non-faceted patterns, including cellular and dendrites, have been extensively advanced thanks to our new capabilities in experimental techniques (e.g. *in situ* X-ray radiography [5] and tomography [6–8]) and numerical simulations [9]. However, faceted patterns, which many intermetallic compounds (IMCs) grow into, have received much less attention. Regardless, faceted IMCs are of significance, impacting both the mechanical and functional properties of materials. For instance, in aluminium alloys, many faceted particles including plate-like $Al_{13}Fe_4$ [10,11], I-shaped Al_3Ni [12], polyhedron Al_6Mn [13] and Al_2Cu [14], could form, all of which play an important role on the mechanical and corrosion properties of Al alloys [15,16].

One interesting phenomenon regarding faceted crystals is the formation of faceted dendrites observed in various alloy systems, such as Cu_6Sn_5 in Sn-4.2Cu alloy [17], I-AlMnBe phases in Al-6Mn-2.5Be alloy [18] and Al_3Sc in Al-2wt%Sc alloy [19]. Regarding the dendritic growth mechanism, the classic view is a morphological instability of the solid-liquid interface that develops into dendritic shapes with branches along preferred crystallographic directions [2]. However, these mechanisms may not be applicable to faceted crystals due to their highly anisotropic crystal growth kinetics. Previous studies proposed a twin-related re-entrant edge mechanism to explain the growth of faceted Silicon [20,21], Germanium [22] and $Al_{13}Fe_4$intermetallic [10], all with plate-lets morphologies. However, whether this mechanism can be applied to faceted dendrites is still unknown and many crystals do not form twins during formation. Al_2Cu is a typical intermetallic formed in Al-Cu based alloys. It has a body centre tetragonal crystal structure ($a = b = 0.6063$nm, $c = 0.4872$nm) [23]. Previous studies have shown that it can grow into L-shape, and hollow-rectangularand dendritic shape [24–27]. We also observed L-shape, and dendritic

* Corresponding author.
E-mail address: b.cai@bham.ac.uk (B. Cai).

https://doi.org/10.1016/j.actamat.2022.117903

Al_2Cu patterns in an Al-45wt%Cu sample melt and solidified in a differential scanning calorimetry (see the supplementary figure s1). However, not much work has been done to understand the transitions between these growth patterns, and the mechanism for the formation of dendritic Al_2Cu has not been clearly elaborated.

The morphologies of IMCs are influenced by external growth conditions [28], including temperature gradients, cooling profiles and magnetic fields. In recent decades, magnetic fields have been proposed as an efficient method to alter the solidification microstructures. The mechanisms are mainly based on magnetohydrodynamics (MHD), which includes magnetic damping, magnetic stirring and thermoelectric magnetohydrodynamics. Under a static magnetic field, magnetic damping is the interaction between the applied magnetic field and fluid flows, which can generate Lorentz force to slow down the fluid flows [29]. The interaction between the thermoelectric currents (due to Seebeck effect) and applied magnetic field can also produce Lorentz force but generate flows [30–33]. This effect is contrary to magnetic damping. For an alternating magnetic fields, magnetic stirring [34] can be induced that may cause temperature and concentration fluctuation in the melt. Recent work shows that MHD effects can be controlled in various solidification settings, from driving solute segregation via thermoelectric effect, to solute mixing and microstructure refinement via magnetic stirring [35]. Magnetic fields have also been shown to influence the growth morphology of Al_2Cu intermetallic. Under a high axial magnetic field (up to 12 T), Li et al. demonstrated that the Al_2Cu crystals were oriented with the <001>-crystal direction along the magnetic field [36]. Wang et al. revealed the structure refinement of Al_2Cu phase during directional solidification under a high (12T) magnetic field [30]. Li et al. [25] shows that a significant axial macrosegregation of the primary Al_2Cu was formed under a static transverse magnetic field during directional solidification. However, the effect of sample rotation under magnetic fields on Al_2Cu crystal formation has rarely been studied.

High-speed X-ray tomography (recording tomograms in seconds or less) has advanced our understanding of nucleation, growth and coarsening of non-faceted crystals during alloy solidification [6,37,38], and recently, it has been applied to study faceted Si [39] and $Al_{13}Fe_4$ particles [11] in Al alloys. Here we used high-speed synchrotron X-ray tomography to study the growth of faceted Al_2Cu crystals under various solidification conditions including upwards and downwards solidification, and rotational solidification under magnetic fields. This work generates fresh insights into the growth mechanisms of faceted crystals, also discusses how the thermo-solute flow, including magnet field-driven flow, influences the microstructures during solidification.

2. Materials and Methods

2.1. Sample preparation

The Al-45wt%Cu master alloy was used in this study. Cylindrical specimens with a diameter of 1.8 mm and length of 100 mm were machined via a wire electrical discharge machining.

2.2. In-situ synchrotron X-ray tomography

A bespoke temperature gradient stage [35] (supplementary figure s2) was used to control the melting and solidification of the Al-45wt%Cu sample, which can be coupled with high-speed synchrotron tomography to capture solidification processes *in situ* and in real-time. As shown in ref [35], two heaters were used to apply a temperature gradient to the sample, allowing directional solidification. The samples were heated up until fully melt under an applied vertical temperature gradient, then held for another 10 min to achieve a steady state condition. The solidification experiments were carried out via cooling both heaters at a constant predefined cooling rate (CR) while keeping the temperature gradient (TG). A transverse static magnetic field with a strength of B = 0.5 T using a permanent magnetic yoke can also be applied to the sample [35]. The distribution of the magnetic flux density surrounding the sample is around 0.5 T (supplementary figure s3). Six experiments were performed with different solidification conditions as shown in Table 1. A positive temperature gradient (TG) means that the top furnace is hotter than the bottom one, which allows upwards solidification, whereas a negative TG means the bottom furnace is hotter, allowing downwards solidification. Fig. 1 discloses the overview of Al_2Cu IMCs from the 6 experiments, which shows that Al_2Cu grew into significantly different morphologies under different solidification conditions.

Table 1
Solidification conditions.

Sample	CR	TG	B = 0.5 T
A	0.05 °C/s	0 °C/mm	No
B	0.05 °C/s	-4 °C/mm	No
C	0.05 °C/s	7 °C/mm	No
D	0.05 °C /s	0 °C/mm	Yes
E	0.02 °C/s	7 °C/mm	Yes
F	0.05 °C/s	7 °C/mm	Yes

The *in situ* solidification experiment was performed at I12 beamline, Diamond Light Source [40] using a 53keV monochromatic X-ray beam. During the solidification process, a high-speed camera (PCO.edge) was set to obtain the tomograms in 5 seconds over 180 every 10 seconds, while the sample was rotating continuously. The images were cropped to 1600×1600 pixels. Each tomography consisted of 1000 projections. Savu system [41] was used to reconstruct the tomograms. The reconstructed volume has a voxel size of 3.24 μm^3.

2.3. Image processing

The 3D images were analysed by Avizo2020.1 (ThermoFisher Scientific, USA). To segment the Al_2Cu crystals, a 3D anisotropic diffusion filter, followed by interactive thresholding was used. The thresholding values were chosen based on the Otsu's method [42] from Image J (see the supplemental note for details).

3. Results and discussion

3.1. Overall microstructural evolution

3.1.1. Solidification without magnetic fields

Fig. 2-a (video 1-a) shows the volume rendered Al_2Cu phase after segmentation at different time stamps solidified under condition A (CR = 0.05 °C/s, TG = 0 °C/mm, B = 0T). t_{a0} is the first time when the IMCs appeared in the field of view (FOV). The IMCs nucleated at the sample surface (Fig. 2-a1). It grew horizontally towards the other side of the sample (video 1-a), then into a dendritic shape (Fig. 2-a2). Later, more crystals formed and grew in different directions to fill the space (from Fig. 2-a3 to a5). A few different morphologies were identified. One is the equiaxed-prism, which has a quasi-equiaxed cross-section plane while a prism structure in the through-thickness direction (marked by the red circle in Fig. 2-a3). L-shaped patterns were formed near the edge of the sample (indicated by black arrows in Fig. 2-a5). L-shaped particles refer to the long rod-like particle whose cross-section perpendicular to the growth direction is L-shaped. A hollow-rectangular pattern (marked by the red arrow) was observed which impinged into the equiaxed-prism structure in Fig. 2-a5. The hollow-rectangular particles refer to the elongated particle whose cross-section is hollow-rectangular.

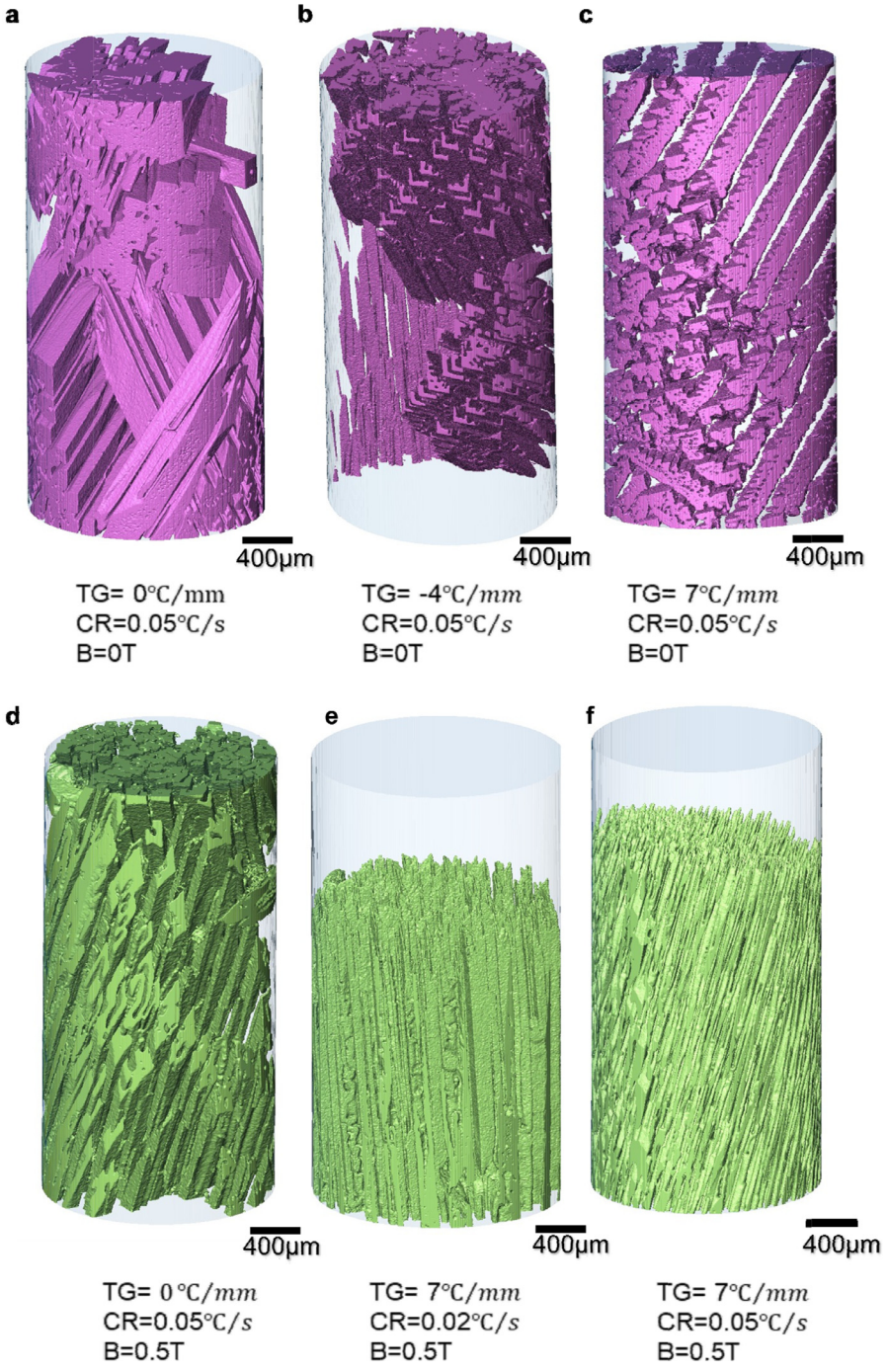

Fig. 1. Overview of Al_2Cu intermetallic compounds in six experiments (a-c) without magnetic field; (d-f) with a transverse magnetic field of 0.5T.

The downwardly solidifying microstructure under condition B (CR = 0.05 °C/s, TG = -4 °C/mm, B = 0T) is shown in Fig. 2-b (video 1-b). Here, multiple highly ordered L-shaped Al_2Cu were formed on the upper side of the FOV (Fig. 2-b1), which then grew downwards, into faceted dendritic structures with secondary arms (pointed by orange arrows in Fig. 2-b2 and b3). Another two new dendrites with the same orientation were formed in the middle region (marked by the red circle). Most of the primary dendrites tilted by about 40° from the vertical direction. However, in the left region of the sample, at the later stage of solidification, a cluster of L-shaped patterns grew downwards almost parallel to the vertical direction.

Fig. 2-c (video 1-c) shows the upward growth (growth rate of 7.7±0.3 μm/s) of Al_2Cu from the experiment C (CR = 0.05 °C/s, TG = 7 °C/mm, B = 0T). The growth rate was calculated based on stabilized overall growth rates of Al_2Cu intermetallic compounds in the vertical direction (see the supplementary note). Two distinctive morphologies were observed: L-shaped (within the red circle in Fig. 2-c5) and dendrites. The columnar faceted dendritic patterns (e.g. marked by the black arrows) have plate-shaped primary stems and small secondary arms with faceted planes and sharp corners. Around 11 dendrites, parallel to each other, tilted by about 30° from the vertical direction, were found. The dendrites observed are asymmetric. One side of the dendrite

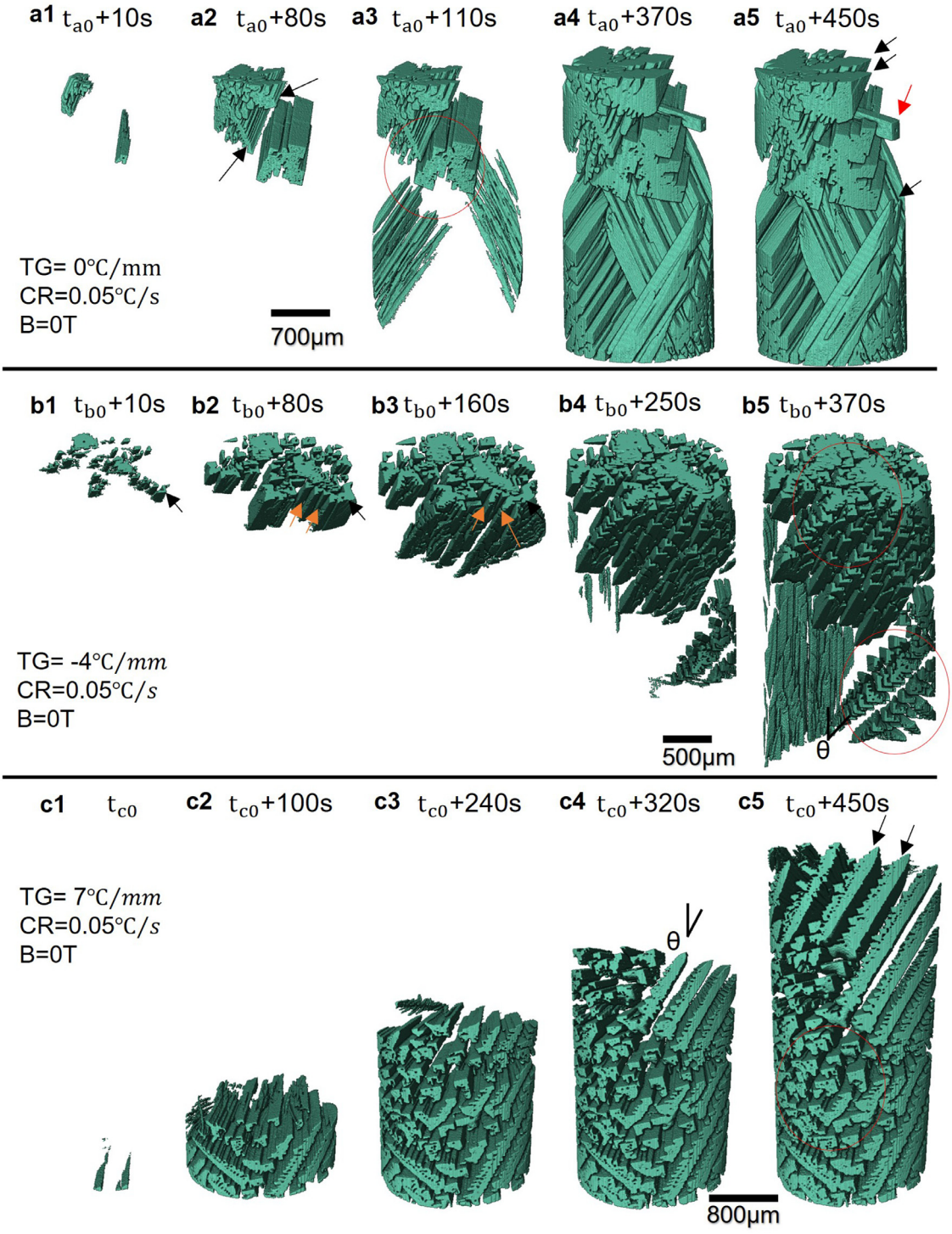

Fig. 2. 3D rendered volume of Al2Cu phase at different timestamp under solidification (a) conditions of A (CR = 0.05 °C/s,TG = 0 °C/mm and B = 0T); (b) condition B (CR = 0.05 °C/s,TG = -4 °C/mm and B = 0T); (c) condition C (CR = 0.05 °C/s,TG = 7 °C/mm and B = 0T).

has multiple secondary branches, while the other side is almost flat.

3.1.2. Solidification under magnetic fields

Three more experiments were performed to study the influence of the 0.5 T magnetic field on the morphology of Al_2Cu IMCs. A static transverse magnetic field (B = 0.5T) was imposed while the sample was rotating for recording X-ray tomograms.

The formation of Al_2Cu under condition D (CR = 0.05 C/s, TG = 0 C/mm, B = 0.5T) is shown in Fig. 3-a (video 2-a).The Al_2Cu compounds appeared first at the top region of the FOV (Fig. 3-a1), leading to the formation of a cluster of faceted dendrites (Fig. 3-a2). The growth direction of L-shaped patterns was no longer orientated to the transverse direction (Fig. 3-a3), different from condition A under similar solidification condition but without the imposed magnetic field.

Fig. 3-b (video 2-b) shows the upwards growth of Al_2Cu under solidification condition E (CR = 0.02 °C/s, TG = 7 °C/mm, B = 0.5T). Multiple L-shape, U-shape and hollow-rectangular patterns (Fig. 3-b2 to 3-b3) grew almost parallel to the vertical direction (z). The

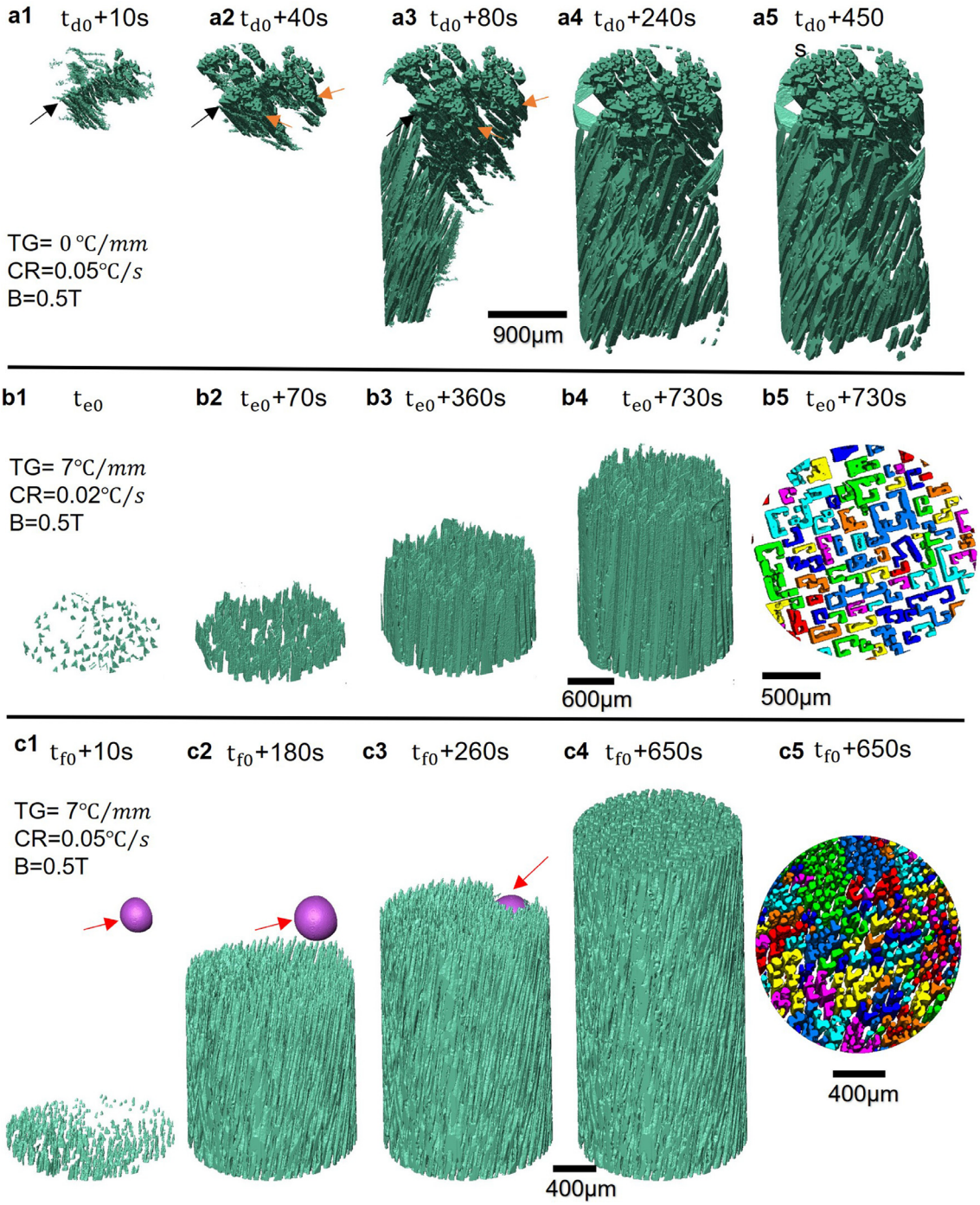

Fig. 3. 3D rendered volume of Al2Cu phase at different timestamp under solidification condition D (CR = 0.05 °C/s,TG = 0 °C/mm and B = 0.5T); (b) condition E (CR = 0.02 C/s,TG = 7 C/mm and B = 0.5T); (c) condition F (CR = 0.05 C/s,TG = 7 C/mm and B = 0.5T).

stabilized growth rate is about 3.5±0.2 μm/s.No faceted dendritic patterns were observed. The well-aligned growth of the IMCs along the vertical direction (z), which were different from sample C, indicates the heat flow in the melt had been modulated because of the imposition of the magnetic field. This also indicates there was no longer a horizontal temperature distribution under condition E. Furthermore, the size of the intermetallic of sample E ($9.5 \times 10^3 \pm 650$ μm^2 in area was 20 times smaller than that of sample C ($2.07\times 10^5 \pm 34000$ μm^2), and the primary pattern spacing was reduced. To calculate the primary dendrite arm spacing [43], we used:

$$\lambda = c\sqrt{\frac{A}{N}} \tag{1}$$

Where λ is the distance between each pattern, c is the coefficient that depends on its microstructure, 0.5 is chosen for a random array of points, and A is the selected area, and N *is* the number of patterns in the selected area. The primary pattern spacing is calculated to be 142.7μm.

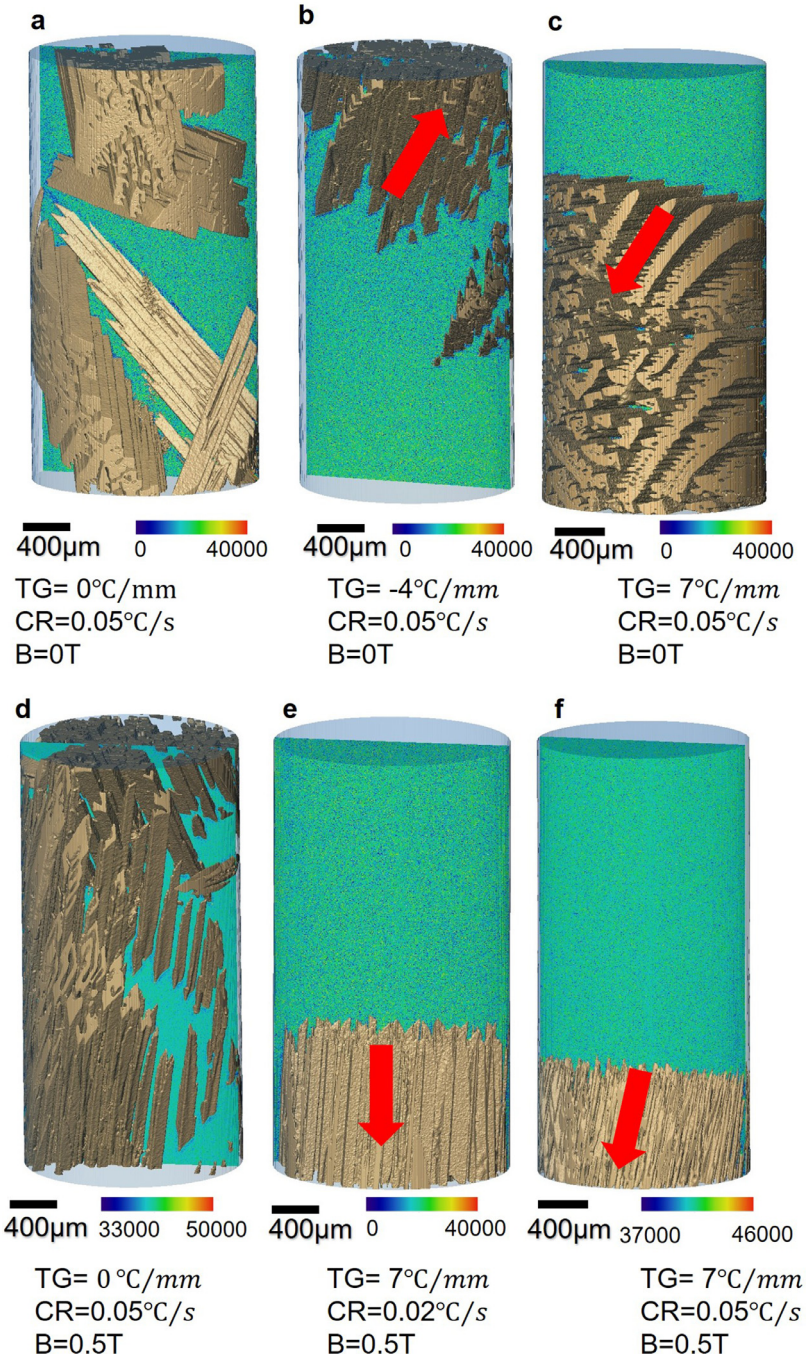

Fig. 4. (a-f) Composition distributions in six experiments.

The growth process of Al_2Cu under solidification condition F (CR = 0.05 °C/s, TG = 7 °C/mm, B = 0.5T) is displayed in Fig. 3-c (video 2-c). Many fine L or U shape Al_2Cu IMCs grew upwards at a rate of about 9.9 ± 0.1 μm/s Fig. 3-c1), well-aligned along the z-direction with a slight tilt. A few non-faceted long cylinder-like IMCs were observed as well (Fig. 3-c5) at the later stage of the solidification. Levelled solid/liquid front can be observed as shown in Fig. 3-c2 and c3. The primary pattern spacing reduced from 142.7μm (sample E) to 88.4μm (sample F), as the number of IMCs increased from 99 to 224. A spherical pore was also observed (purple coloured in Fig. 3-c1, c2 and c3). Due to phase-contrast effect [44], the fringes at the edges of the pore were bright and have similar contrast as Al_2Cu. The pore was formed during the cooling process in the melt (in video 2-c), which highly likely because that hydrogen tended to escape from the solution and form bubbles during solidification [45].

3.1.3. Heat flows and the effects of the magnetic field

It is known that the heat flow has a strong influence on the growth orientations of Al_2Cu intermetallic [46]. Hence the growth direction of Al_2Cu observed allows us to determine the heat flow direction of the sample during the experiments.

Under solidification condition A, B and C, the orientation of the faceted dendrites is controlled by a heat flow resulted from the combination of vertical and horizontal temperature gradients. For sample A, which did not apply vertical temperature gradient but has a horizontal temperature gradient, a prism with an equiaxed shape formed, elongated along the horizontal temperature gradi-

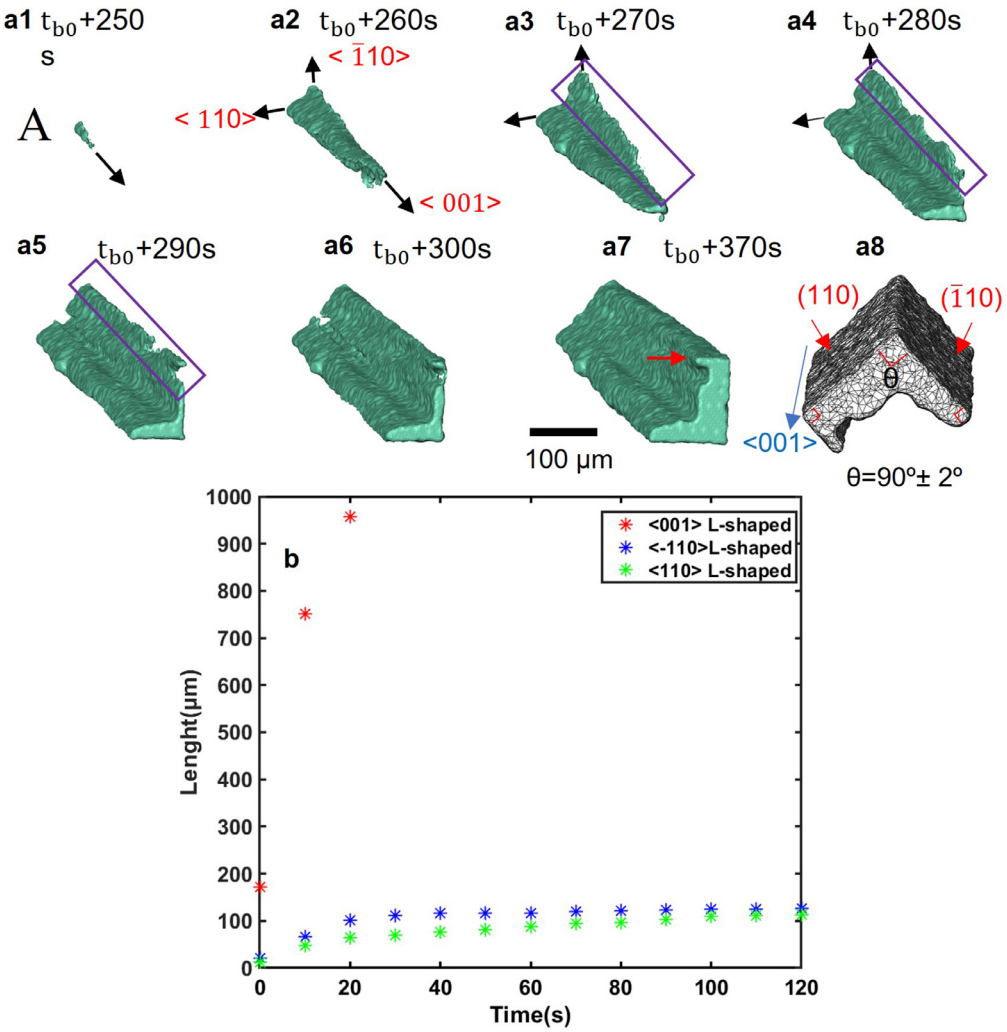

Fig. 5. (a1-a7) Selected L-shaped pattern from solidification condition B (CR = 0.05 C/s,TG = -4 C/mm and B = 0T); (a8) angles between different facets of L-shaped pattern; (b) Growth length according to its crystallographic directions from (a8).

ent, as shown in Fig. 4-a. There were a few randomly oriented crystals, indicating that the heat flow is rather complicated and non-directional. For sample B, which has a vertical temperature gradient of -4 °C/mm, the crystals grew downwards, titled about 40° from the vertical direction, as shown in Fig. 4-b. For sample C, when applying a vertical temperature gradient of 7 °C/mm, the crystals grew upwards, tilted about 30° respecting to the vertical direction in Fig. 4-c. The tilted growth of crystals suggests that the heat flow deviated from the vertical direction. Possible heat flow directions are indicated by the red arrows in Fig. 4-b and 4-c for the two samples.

It is also noted that sample A, B and C were rotated. Here, we used the grey values of the tomograms to indicate and map the composition distribution as shown in Fig. 4a-4c (videos 9-a to 9-c). No macro-segregation was observed, which suggests that sample rotation did not cause solute segregation in the melt during solidification. A previous study [47] shows that when using the accelerated crucible rotation technique to spin up the melt from static to a high rotation speed such as 60 rpm, the flows were stirred by produced a shearing of the solution. In our experiments, after the sample was accelerated from static to a slower rotation speed of $\omega = \pi/5$ rad/s, it was held and rotating at this speed for another 10 minutes to achieve a steady-state condition before cooling. Therefore, the accelerated effect can be neglected.

The temperature gradient and cooling rate between sample C (CR = 0.05 °C/*s*,TG = 7 °C/*mm* and B = 0T) and F (CR = 0.05 °C/*s*,TG = 7 °C/*mm* and B = 0.5T) are the same. But sample F was rotated in a magnetic field of 0.5 T during solidification, while sample C was not. Al_2Cu crystals formed in sample F were all basic unit shapes – fine, elongated and aligned well along the vertical direction, significant different from sample C (tilted, coarse plate-like columnar dendrites). This indicates that the heat flow direction in sample F was along the vertical direction (indicated by the red arrow in Fig. 4-f) and there was no horizontal heat flow. It is likely that when rotating the melted Al-45wt%Cu in a static transversal magnetic field, a rotational flow on the horizontal plane could have been induced that homogenized the horizontal temperature gradient. A rotational flow or even swirling flow has already been proven to be induced under similar conditions numerically in our previous work [35].

The elimination of horizontal temperature gradients shows that an additional rotational flow might be induced in the transverse plane that homogenized the temperature. The question is what drives the flow. Our previous work [35] has shown that when rotating the directional solidifying samples inside a magnetic field, it can cause both electromagnetic stirring (EMS) and thermoelectric (TE) magnetic convection, both of which can induce flows in the mushy zone and the liquid zone. The strength of EMS is mainly determined by the sample rotation speed and magnetic

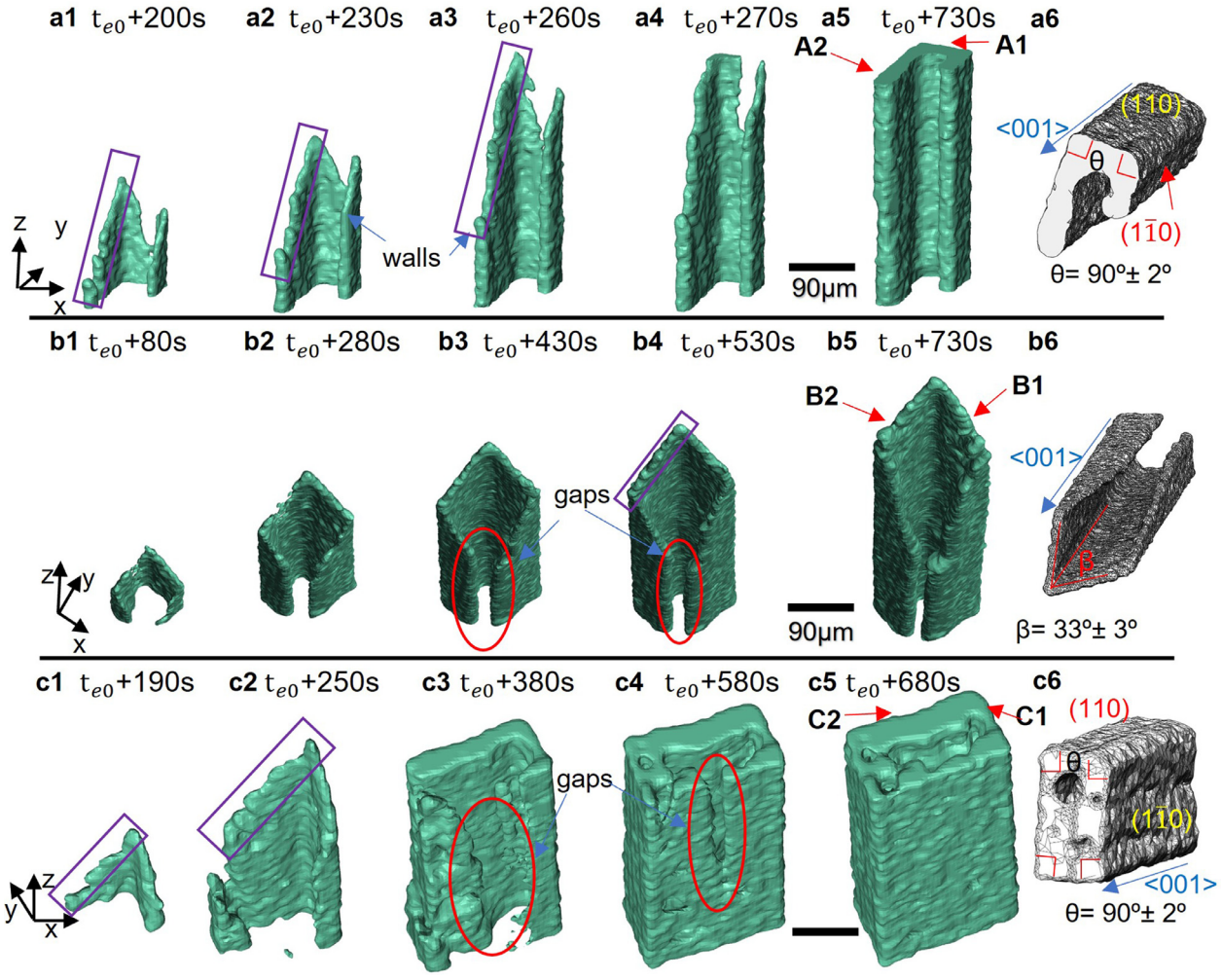

Fig. 6. Formation process of selected (a1-a5) U-shaped pattern; (b1-b5) nearly hollow-rectangular and (c1-c5) hollow-rectangular pattern; (a6, b6 and c6) bounding facets and growth directions of Al_2Cu crystals.

field strength, both of which are the same for samples D, E and F. Therefore, if EMS was the controlling mechanism that drove the flow, the microstructure modification would be the same for D, E, and F samples. However, in our experiments, the substantial refinement of Al_2Cu was only observed in sample E and F when a temperature gradient was applied, but not in sample D. TE magnetic convection, on the other hand, is strongly related to the temperature gradient as TE currents $= S\nabla T$ (where S is the Seebeck coefficient and ∇T is the temperature gradient). This indicates that TE magnetic convection might prevail in the sample E and F as the controlling mechanism that drives the flow. This peculiar flow might also push the solute out of the mushy zone, likely resulting in a homogenised solute layer above the solid-liquid interface absent of segregation [35]. Li et al. [25] carried out directional solidification experiments on Al-40wt%Cu alloys under a static transverse magnetic field of 0.5 T (noted their samples were not rotated). They found out that an axial macro segregation zone was formed, attributed to the TE magnetic convection [25]. Their work shows that TE magnetic convection can cause the redistribution of solutes. In Fig. 4-e and f (videos 9-e and f), macro-segregation was absent suggesting that rotating the sample within the 0.5 T magnetic field did not cause solute segregation.

It is less clear about what has caused the significant structure refinement. Wang et al. [30] showed that dislocations formed in Al_2Cu in directionally solidified Al-40wt%Cu under a 12 T magnetic field. They suggested that TEMF in solid Al_2Cu led to the dislocation multiplication and dendrite fragmentation during solidification, which is the main mechanism they proposed for the refinement of the structures. However, the effect of solute redistribution due to the very strong magnetic field on Al_2Cu refinement was not discussed. Cai et al. [35] showed that via simulation, on an Al-Si-Cu alloy, EMS and TEMHD combined flows in the melt can be controlled in a way to significantly refine microstructures during direction solidification. In this study, we suspect that the stirring flow caused by rotating the sample under a transversal magnetic field drive the solute from the mushy region, leading to the depletion of solute there and a decrease of the dendrite spacing. The next step would be to perform numerical simulations on hypereutectic Al-Cu alloys as in ref [35] to determine the flow conditions. Experimentally, it would be necessary to develop methods to measure the magnetic field-driven flow as well.

3.2. Morphologies of Al_2Cu IMCs

From the six experiments, it can be shown that most of Al_2Cu crystals have a rod-like shape with L,Uand hollow-rectangular cross-section, which we categorized as basic units. A few crystals have faceted dendritic patterns. To further investigate the development of these morphologies during solidification, we obtained some representatives of the compounds, as shown from Fig. 5 to 10.

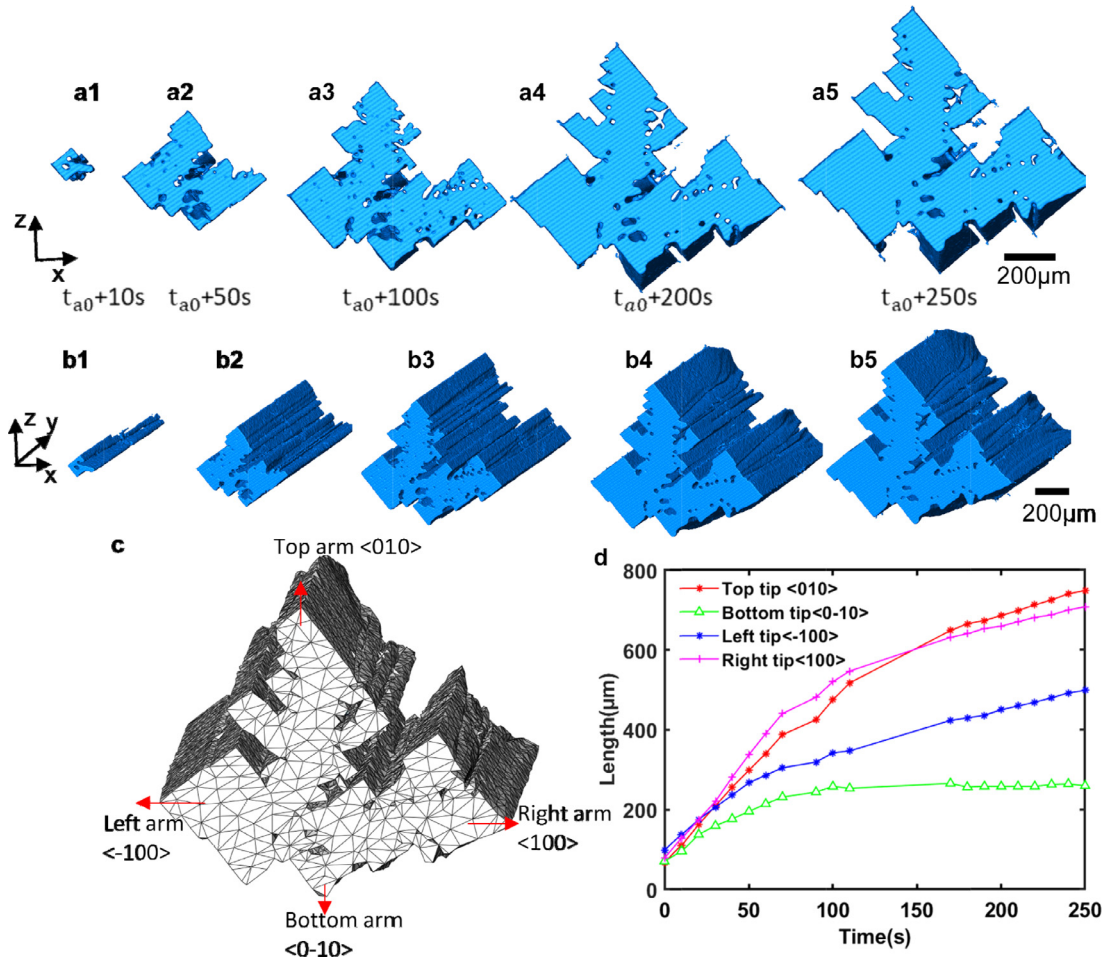

Fig. 7. Selected dendrite pattern from Fig. 2-a solidification condition A (CR = 0.05 C/s,TG = 0 C/mm and B = 0T); (a) Front view of faceted equiaxed-prism structure at different time without temperature gradient; (b) Side view of faceted equiaxed-prism structure at different time without temperature gradient; (c) Meshed equiaxed-prism Al2Cu intermetallic; (d) Length of the equiaxed structure as a function of time.

3.2.1. Basic units

Fig. 5(video 3) presents the growth of one L-shaped pattern from t_{b0}+250s to t_{b0}+370s extracted from sample B. A small rod-like pattern (Fig. 5-a1) first appeared. Then it grew longer and formed two branches perpendicular to each other within 10 s (and 5-a2). The growth directions of the branches are marked by the black arrows. After another 10 s, the rod became longer, and the branches grew thick too (Fig. 5-a3). The branches extended further in Fig. 5-a4 and 5-a5, forming the L-shaped pattern. It continued to thicken at the later stage of solidification while the overall Lshape was maintained. A fin (pointed by the red arrowin Fig. 5-a7) formed on one of the branches, oriented perpendicular to that branch.

The bounding facets of Al_2Cu intermetallic in an Al-Cu alloy are {110} planes, as these planes require the lowest attachment energy [24,46]. Al_2Cu phase also has a strong crystalline anisotropy and a preferred growth direction along <001> [24]. EBSD analysis of the basic unit was also performed which reveals the preferred growth directionis <001>. Details are shown in the supplementary note 6. The angle between the adjacent facets of the bounding wall of the basic L unit patterns was measured to be 90°±2° (Fig. 5-a8). This suggests that the facets are {110} of Al_2Cu. Hence the bounding planes {110} and growth direction <001> of the selected L shaped crystal can be indexed (Fig. 4-a8). The growth length as a function of time according to its crystallographic direction are quantified and plotted in Fig. 4-b. In <001> direction, the intermetallic reached a high growth rate of 39.2$\mu m/s$ in the first 20 seconds, while the branches grew slowly at a rate of 3.0$\mu m/s$ in the direction of <-110> and 1.9 $\mu m/s$ in the direction of <110> in the first 30 seconds. They then barely grew once the L-shaped was formed.

The growth process of U-shaped Al_2Cu, extracted from experiment E is shown in Fig. 6-a (video 4-a). This crystal grew to be very long, so only a part of the crystals was cropped to show in the figures. The crystal had cuspidal growth fronts (Fig. 6-a1 and a2). The gap between the side walls became smaller due to the thickening of the side walls(Fig. 6-a4 and 6-a5).The bounding facets of this crystal are also {110} planes and indexed as shown in Fig. 6-a6.

The growth processes of two hollow-rectangular Al_2Cu IMCs are shown in Fig. 6-b (video 4-b) and 6-c (video 4-c). The crystals grew along <001> at a growth rate of about 3.3 $\mu m/s$ to an elongated rectangular shape with a central rectangular hole. The growth fronts of both crystals were also cuspidal (Fig. 6-b2 to b5 and Fig. 6-c2), with bounding facets forming an angle of 33°±3° with the <001> growth direction (Fig. 6-b6). The crystal in Fig. 6-b grew into a nearly hollow-rectangular shape but still had a gap on one of its walls. The crystal in Fig. 6-c transited from an L-shaped pattern (Fig. 6-c2) to U-shaped (Fig. 6-c3) and finally a hollow-rectangular structure (Fig. 6-c5). The closure of the gap on the wall (Fig. 6-c3 to c5) led to the final hollow rectangular shape. The growth length according to its crystallographic directions of the basic units as a function of the growth time are shown in the supplementary figure-s5.

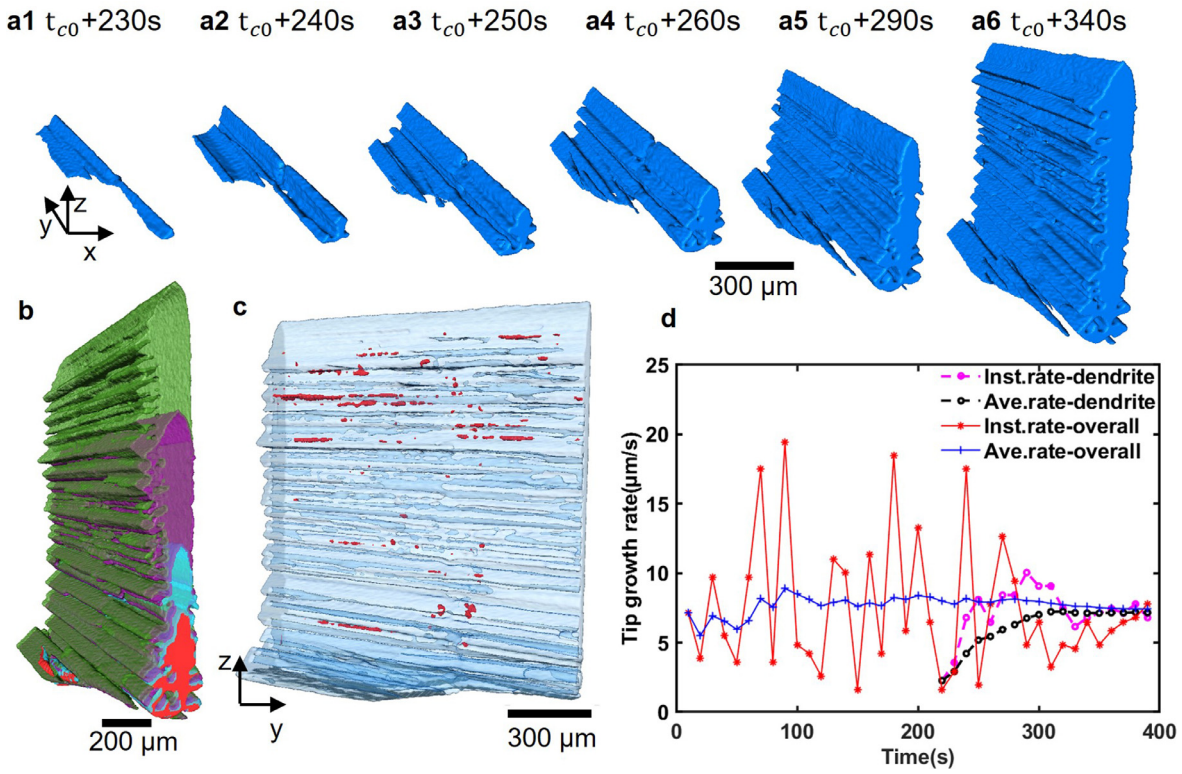

Fig. 8. Selected columnar dendrite from Fig. 2-c under solidification condition C (CR = 0.05 C/s,TG = 7 C/mm and B = 0T); (a1-a6) Volume rendering of a single dendrite with solidification time; (b) Transparent overlapped view of the dendrite at t_c0+270 s, t_c0+290 s, t_c0+340 s,t_c0+390 s; (c) Internal defects at t_c0+390s front view; (d) Average and instantaneo tip growth rates of the overall crystal array and the single dendrite of figure a.

3.2.2. Dendrites

Fig. 7 (video 5) shows the growth process of the equiaxed-prism Al_2Cu IMC, extracted from sample A (Fig. 2-a). The crystal grew into equiaxed-like shape in the x-z plane (Fig. 7-a), whereas it grew as a prism along y-direction (Fig. 7-b). This is different from typical equiaxed patterns that proceed equally in all directions [48]. Here, a rectangular-shape basic unit first appeared (Fig. 7-b1). Then it extended along its four corners (Fig. 7-a2), forming four arms around the core, three of which were dendritic shape. The growth of the left and bottom arms was constrained (Fig. 7-c) due to the limited space available for growth. Only the top and right tips were able to grow into large size as shown in Fig. 7-a3 to a5.The meshed 3D volume of the equiaxed-prism structure (Fig. 7-c) shows that the angles between bounding adjacent planes are all around 90º. EBSD analysis was implemented to determine the crystallographic planes of the faceted dendritic structure of one post-solidification sample (Details can be found in the supplementary note 6), which shows the tip growth planes are {100} or {010}. Different from the dendrite arms in typical non-faceted dendrites, which form parabolic tips [6,7,49], the arm of the Al_2Cu dendrite is flat with sharp corners (Fig. 7-c). Fig. 7-d presents the length of the four dendrite arms as a function of time. The length of the crystal arms increased almost linearly in the first 70 seconds. The growth speed slows down afterwards. The bottom tip almost stopped to grow as there was no more available space nearby. The other three arms continued to grow and the left-arm reached a length of 500μm, while the right and top arms have the greatest dimensions of around 750μm.

Fig. 8-a1 to a6 (video-6a) show the growth of a single large columnar dendrite from t_{c0}+230s to t_{c0}+340s, extracted from sample C (figure2-c). Fig. 8-b shows the overlapped images of the same dendrite at different time points. The growth started from a faceted crystal tip (Fig. 8-a1), which grew in horizontal y-direction until it reached the sample surface. It then extended in z-direction (Fig. 8-a2), while secondary arms appeared in x-direction (Fig. 8-a3). Additionally, gaps and internal holes (which are filled with melt during solidification) occurred at the interfaces between neighbouring secondary arms (Fig. 8-c, red colour). Fig. 8-d shows the instantaneous and average growth rates of the whole sample C (Fig. 2-c) and the selected asymmetric dendrite. The positions of the dendrite tips were first measured in all tomograms. The instantaneous growth rate is the difference of dendrite tip positions between two consecutive tomograms divided by the time interval (10 s). The average rate is the tip position of the dendrites divided by the total solidification time. The instantaneous tip growth rate of the whole sample is fluctuating in a periodical manner, whereas the average growth rate kept at around 7.7±0.3μm/s, which is because a constant temperature gradient and cooling rate were applied. The instantaneous growth rate of the selected dendrite is also fluctuating. The average growth rate of the dendrite increased from about 2.2 μm/s to a plateau of 7.2 μm/s within 100 s, indicating that there is a change of growth conditions locally as the dendrite grew. The average tip growth rates of Al_2Cu IMC from experiment E and F are also quantified and shown in supplementary note Fig. 6.

The formation of a symmetric dendrite (I) and an asymmetric dendrite (II) from sample B are shown in Fig. 9-a (front view) and 9-b (rear view). Dendrite I appeared before the dendrite II. The secondary arms of the dendrite I were branching in both directions perpendicular to the primary arm, forming a symmetric dendrite. Tertiary arms can also be found at later stage of solidification. However, the secondary arms of the dendrite II branched only on one side, f orming an asymmetric dendrite. The formation of asymmetric dendrites is common when two or multiple dendrites grow together and compete for space and solute to grow. This has also been observed in non-faceted dendrites [6]. What is also no-

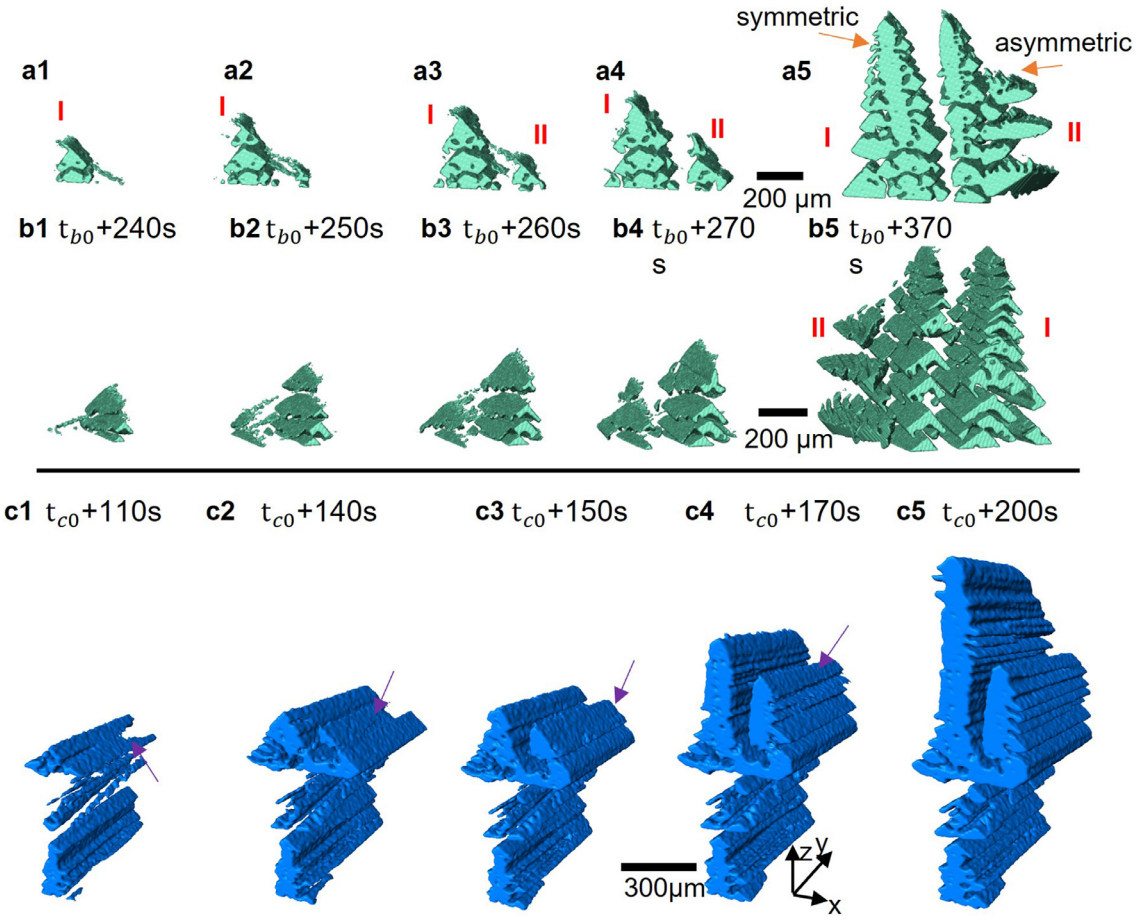

Fig. 9. Selected pattern from Fig. 2-b under solidification condition B (CR = 0.05 C/s,TG = -4 Cmm and B = 0T): (a1-b5) showing the growth of a symmetric and asymmetric faceted dendrites; (a1-a5) front view, (b1-b5) back view; Selected pattern from Figure 2-c under solidification condition C (CR = 0.05 Cs,TG = 7 C/mm and B = 0T): (c1-c5) showing the growth of a tertiary arm into a dendrite.

ticeable is that it seems both dendrites were composed of many L-shaped elongated basic units, which is clearly demonstrated in the rear view (Fig. 9-b and video 7-b).We also observed a tertiary arm grew into a new primary dendrite (Fig. 9-c and video 7-c). As shown in Fig. 9-c1, a secondary branch formed first (marked by the purple arrow). Then a tertiary arm formed on the top of the secondary branch (Fig. 9-c2 and c3), growing upwards into a well-developed asymmetric dendrite (Fig. 9-c5).

3.2.3. Coalescence and coarsening

The coalescing behaviours of nearby IMCs can be observed in Fig. 10-a (video 8-a).As highlighted by the red circle in Fig. 10-a1, two L-shape patterns were initially separated. As the solidification proceeded, the walls of the two crystals coarsened and coalesced to form a thicker single wall as shown in Fig. 10-a2 to 10-a6, highly likely sharing a common crystallographic plane.

Fig. 10-a also shows that several IMCs transformed from faceted shapes to non-faceted rod-like structures, one of which was extracted and shown in Fig. 10-b (video 8-b). Here, the transition is related to the processes of growth and coarsening or Ostwald ripening of Al_2Cu at the later stage of solidification. A faceted L-shaped pattern was first formed, similar to the one in Fig. 5. However, the concave of the L-shaped pattern, as pointed by black arrows from Fig. 10-b4 to 10-b5, was further filled during the coarsening stage. The driving force of this process is to reduce the total surface free energy [50].

3.2.4. Growth mechanisms of Al_2Cu

According to Jackson's model, if the Jackson roughing factor α value is higher than 2, the crystal would grow into a faceted structure, while a non-faceted structure are expected if it is smaller than 2 [51,52]. Jackson roughing factor for Al_2Cu is around 2.1, hence faceted patterns are expected for Al_2Cu. Governed by the interface attachment kinetics, stepwise lateral growth, where the solid/liquid front advances by lateral motion of the growth steps has been proposed to be the growth mechanism of faceted IMCs such as Al_3Sc [19] and Cu_6Sn_5 [17] at small undercooling. Rough interfaces have been observed from the early growth stages of Al_2Cu, such as Fig. 5 a-1 to a-4 and in Fig. 6 (marked by purple rectangles), which might be evidence of lateral steps.

According to the classic theory of crystallization, the growth of crystal proceeds due to the attachment of atoms from the melt to the surface [53]. Recently, oriented particle attachment via nano-precursor attachment has been proposed as an alternative pathway for crystallization [53,54]. The reduction of total energy is the driving force for crystal growth via oriented particle attachment [55], which comes from the interatomic interactions in the attaching particles, as well as the surface energy of the attaching surfaces [55]. Oriented particle attachment mechanism was proposed in ref [24] to describe the growth mechanism of Al_2Cu. The bonding of Al_2Cu includes Al-Al and Al-Cu covalent bonds [56], which is different from the less directional metallic bonds in α-Al. Hence Al_2Cu intermetallic might grow via oriented particle attachment, rather than classic crystallization. Our work did not provide direct

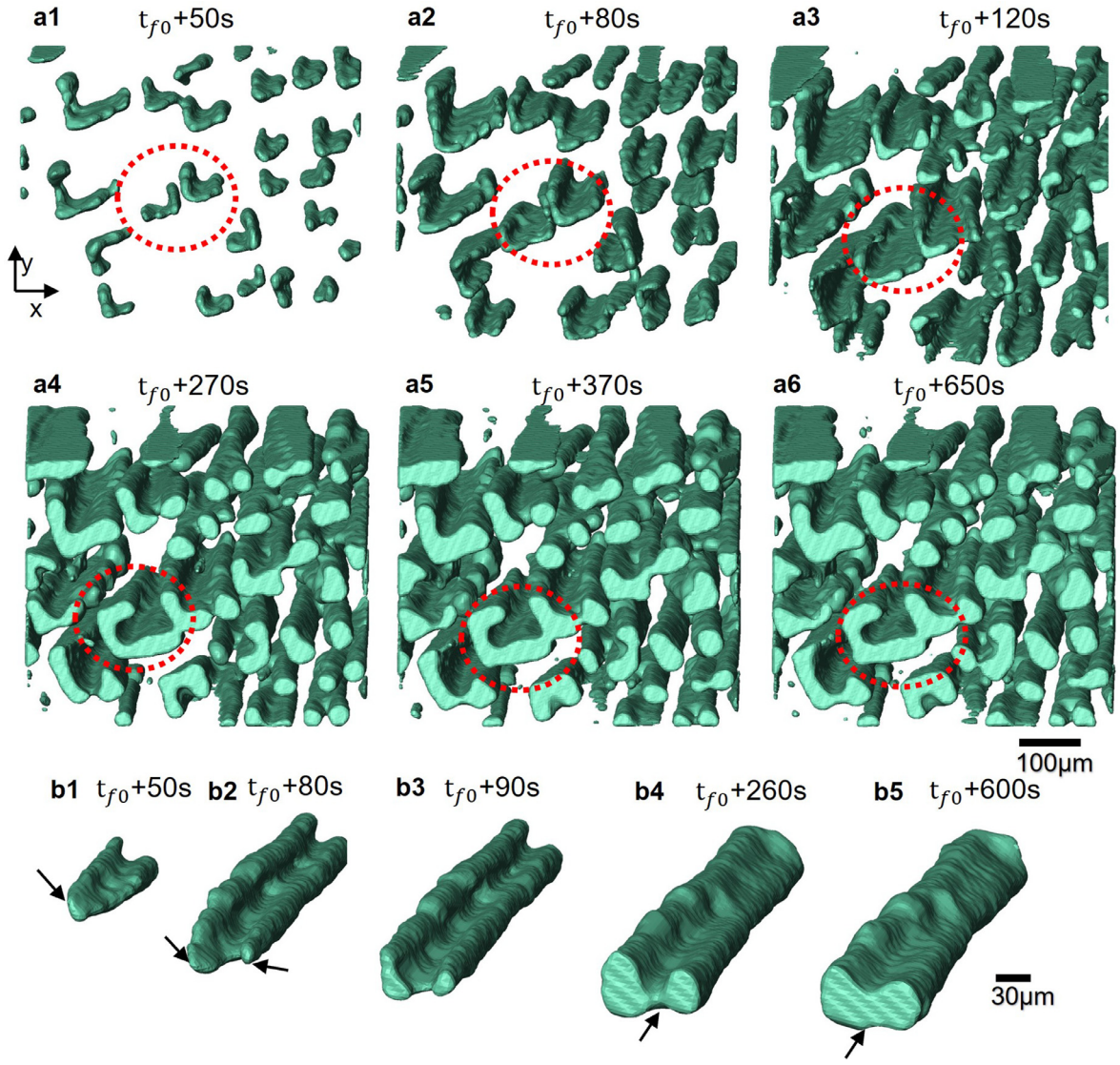

Fig. 10. (a) Formation process of a selected; (b) faceted to non-faceted transition of Al2Cu intermetallic compounds cluster; from Figure 3-c under solidification condition F (CR = 0.05 C/s,TG = 7 C/mm and B = 0.5T).

evidence to support this hypothesis. This is because the resolution of the tomography (3.24 μm^3 voxel size) used does not allow us to observe the attachment of precursors which are usually in nano-size. Hence nano-scale imaging techniques such as *in situ* TEM [57,58] would be a useful tool to be applied to confirm this hypothesis.

Various final morphologies of Al_2Cu (L-shaped, E-shaped, and rectangle) have already been observed in previous studies [26,46,59]. However, the relationship and transitions between these growth patterns have not been experimentally identified. Here, we have shown a clear transition from an L-shaped pattern to U-shaped, and finally to a hollow-rectangular pattern (Fig. 6-b and 6-c). This suggests that L-shapes and U-shapes might be intermediate stages for Al_2Cu growth, whereas the hollow rectangular shapes are the final stage. The transition stages for the basic unit patterns of the Al_2Cu phase is schematically shown in Fig. 11-a.

Two types of faceted dendrites were observed, namely prism-equiaxed and columnar plate shaped. As shown in Fig. 8, the growth of the faceted dendrites seems to be through a self-repeated stacking of L-shaped patterns layer-by-layer. The process is schematically shown in Fig. 11-b. An elongated L shaped particle formedpossibly along <001> direction first due to a horizontal temperature gradient, then new L shaped particles stacked on top of it.As the process repeated and more particles stacked layer-by-layer, a columnar dendrite arm grew upwards. Figs. 8 and 9 show this process clearly, especially in Fig. 9-b. The fact that the concave side of the 'L' always stacked on the convex side indicates that the process is controlled by the crystallographic anisotropy of the Al_2Cu crystal, which minimizes the formation energy and occupies the least space. For the formation of the prism-equiaxed dendrite (Fig. 7-b), an elongated rectangular-shape core (Fig. 7-b1) formed first. L-shaped patterns then attached on the four tips of the core layer-by-layer repeatedly, forming four secondary arms. The final shape of the equiaxed-prism structure is also controlled by space and solute contents available for growth. The classical growth mechanism for dendrites formation states that a morphological instability of the planar solid-liquid interface [6,60], resulted into tip splitting, side-branch protrusions and parabolic tips, which is usually applied to non-faceted dendrites [6] as well as some faceted dendrites [19]. However, this mechanism is not suitable to explain the formation of the faceted dendritic structures of Al_2Cu according to our experimental observation (e.g. no protru-

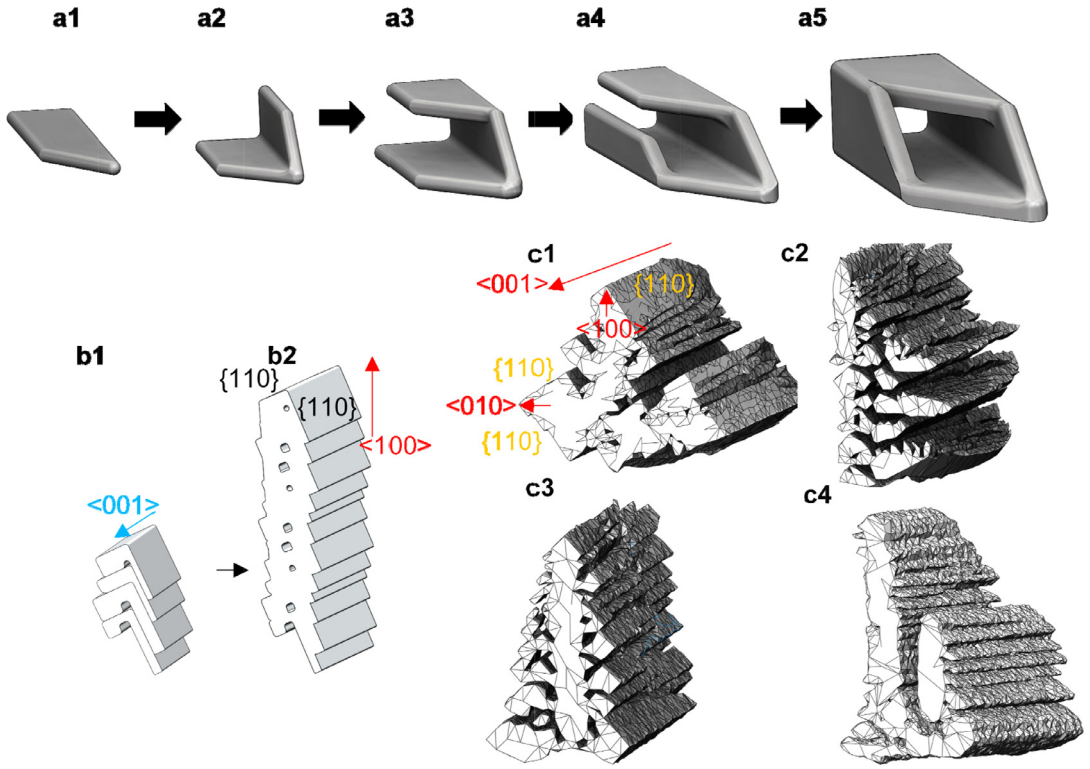

Fig. 11. (a) The schematic diagram of the formation process of basic units; (b1-b2) Schematic diagram of self-repeating layer-by-layer growth mode of Al2Cu phase; (c1) an equiaxed-prism structure; (c2) an asymmetric faceted dendrite; (c3) a symmetric faceted dendrite; (c4) a faceted dendrite with a tertiary arm.

sions were observed during dendrite growth, the tip shape is not parabolic, and the growth direction of the dendrite tip is not the preferred <001> direction). Self-repeated stacking of basic units that leads to faceted dendrite formation could be widely applicable for a range of faceted crystals, such as Cu_6Sn_5 [17], I-AlMnBe [18] and Al_3Sc [19]. But more experimental work and simulation are needed to further validate and confirm this faceted dendrite formation mechanism.

4. Conclusions

In this study, the growth dynamics and mechanisms of the faceted Al_2Cu intermetallic compounds were investigated using high-speed synchrotron X-ray tomography during solidification of Al-45wt%Cu alloy. This works offers a new perspective to understand intermetallic growth during solidification and open the windows for developing new approaches to control, and new models to predict, intermetallic compounds for a wide range of alloys. The following key conclusions can be made.

1. A variety of faceted patterns were found, which can beclassified into two distinctive categories: basic unit shapes and dendrites.
2. The basic unit growth patterns of Al_2Cu are elongated rod-like with an L-shaped, U-shaped, or hollow-rectangular cross-section. A transition process from L-shape to U-shape, and finally to hollow-rectangular shape was observed.
3. Faceted dendritic patterns of Al_2Cu include equiaxed-prism and columnar dendrites (symmetric and asymmetric). The 4D visualization of the growth process of the faceted dendrites suggests that the growth mechanism of the Al_2Cu faceted dendrites is self-repeated layer-by-layer stacking of faceted basic units (such as L-shaped or hollow rectangular patterns), which is different from the interface instability induced dendrite formation.
4. For upward directional solidification of Al-45wt%Cu, when rotating the solidifying sample in a transversal 0.5 T magnetic field, fine and regulated crystal arrays were obtained, much finer than that solidified without the magnetic field. This is attributed to a rotational stirring flow that regulated the heat flow and homogenized the solute distribution. The morphology of faceted Al_2Cu was directly influenced by the thermal profile in the sample. The applied static magnetic field has an indirect impact via promoting fluid flows to change the temperature gradients while the sample was rotating.

Declaration of Competing Interest

The authors declare that they have no known competing financial interests or personal relationships that could have appeared to influence the work reported in this paper.

Acknowledgement

Z.S. thanks the UK-EPSRC CDT Grant (No: EP/L016206/1) in Innovative Metal Processing for financial support. B.C. acknowledges the support from the Alan Turing Fellowship (2018-2021). We thank the Diamond Light Source for providing the beamtime (EE19216–1).

Supplementary materials

Supplementary material associated with this article can be found, in the online version, at doi:10.1016/j.actamat.2022.117903.

References

[1] T. Haxhimali, A. Karma, F. Gonzales, M. Rappaz, Orientation selection in dendritic evolution, Nat. Mater. 5 (2006) 660–664, doi:10.1038/nmat1693.

[2] W. Kurz, M. Rappaz, R. Trivedi, Progress in modelling solidification microstructures in metals and alloys. Part II: dendrites from 2001 to 2018, Int. Mater. Rev. 0 (2020) 1–47, doi:10.1080/09506608.2020.1757894.

[3] M. Sokoluk, C. Cao, S. Pan, X. Li, Nanoparticle-enabled phase control for arc welding of unweldable aluminum alloy 7075, Nat. Commun. 10 (2019) 1–8, doi:10.1038/s41467-018-07989-y.

[4] D.J. Fisher, W. Kurz, A theory of branching limited growth of irregular eutectics, Acta Metall 28 (1980) 777–794, doi:10.1016/0001-6160(80)90155-8.

[5] A.J. Clarke, D. Tourret, Y. Song, S.D. Imhoff, P.J. Gibbs, J.W. Gibbs, K. Fezzaa, A. Karma, Microstructure selection in thin-sample directional solidification of an Al-Cu alloy: In situ X-ray imaging and phase-field simulations, Acta Mater 129 (2017) 203–216, doi:10.1016/j.actamat.2017.02.047.

[6] B. Cai, J. Wang, A. Kao, K. Pericleous, A.B. Phillion, R.C. Atwood, P.D. Lee, 4D synchrotron X-ray tomographic quantification of the transition from cellular to dendrite growth during directional solidification, Acta Mater 117 (2016) 160–169, doi:10.1016/j.actamat.2016.07.002.

[7] N. Limodin, L. Salvo, E. Boller, M. Suéry, M. Felberbaum, S. Gailliègue, K. Madi, In situ and real-time 3-D microtomography investigation of dendritic solidification in an Al-10 wt.% Cu alloy, Acta Mater 57 (2009) 2300–2310, doi:10.1016/j.actamat.2009.01.035.

[8] B. Cai, S. Karagadde, D. Rowley, T.J. Marrow, T. Connolley, P.D. Lee, Time-resolved synchrotron tomographic quantification of deformation-induced flow in a semi-solid equiaxed dendritic Al-Cu alloy, Scr. Mater. 103 (2015) 69–72, doi:10.1016/j.scriptamat.2015.03.011.

[9] W.J. Boettinger, J.A. Warren, C. Beckermann, A. Karma, Phase-field simulation of solidification, Annu. Rev. Mater. Sci. 32 (2002) 163–194, doi:10.1146/annurev.matsci.32.101901.155803.

[10] S. Feng, Y. Cui, E. Liotti, A. Lui, C.M. Gourlay, P.S. Grant, In-situ X-ray radiography of twinned crystal growth of primary Al13Fe4, Scr. Mater. 184 (2020) 57–62, doi:10.1016/j.scriptamat.2020.04.010.

[11] Z. Song, O. Magdysyuk, L. Tang, T. Sparks, B. Cai, Growth Mechanisms of Faceted Al13Fe4 Intermetallic Revealed by High-Speed Synchrotron X-Ray Quantification, J. Alloys Compd. 861 (2021) 1–15 https://doi.org/https://doi.org/10.1016/j.jallcom.2021.158604.

[12] Z. Ding, Q. Hu, W. Lu, N. Zhang, X. Ge, S. Cao, T. Yang, M. Xia, J. Li, Continuous Morphological Transition and Its Mechanism of Al3Ni Phase at the Liquid-Solid Interface During Solidification, Metall. Mater. Trans. A Phys. Metall. Mater. Sci. 50 (2019) 556–561, doi:10.1007/s11661-018-5059-4.

[13] H. Kang, T. Wang, X. Li, Y. Su, J. Guo, H. Fu, Faceted-nonfaceted growth transition and 3-D morphological evolution of primary Al6Mn microcrystals in directionally solidified Al-3 at.% Mn alloy, J. Mater. Res. 29 (2014) 1256–1263, doi:10.1557/jmr.2014.111.

[14] X. Li, Z. Ren, Y. Fautrelle, Y. Zhang, C. Esling, Morphological instabilities and alignment of lamellar eutectics during directional solidification under a strong magnetic field, Acta Mater 58 (2010) 1403–1417, doi:10.1016/j.actamat.2009.10.048.

[15] P. Jarry, M. Rappaz, Recent advances in the metallurgy of aluminium alloys. Part I: Solidification and casting, Comptes Rendus Phys 19 (2018) 672–687, doi:10.1016/j.crhy.2018.09.003.

[16] H. Shi, E.H. Han, F. Liu, T. Wei, Z. Zhu, D. Xu, Study of corrosion inhibition of coupled Al2Cu-Al and Al3Fe-Al by cerium cinnamate using scanning vibrating electrode technique and scanning ion-selective electrode technique, Corros. Sci. 98 (2015) 150–162, doi:10.1016/j.corsci.2015.05.019.

[17] J.W. Xian, S.A. Belyakov, M. Ollivier, K. Nogita, H. Yasuda, C.M. Gourlay, Cu6Sn5 crystal growth mechanisms during solidification of electronic interconnections, Acta Mater 126 (2017) 540–551, doi:10.1016/j.actamat.2016.12.043.

[18] H. Kang, T. Wang, Y. Lu, J. Jie, X. Li, Y. Su, J. Guo, Controllable 3D morphology and growth mechanism of quasicrystalline phase in directionally solidified Al-Mn-Be alloy, J. Mater. Res. 29 (2014) 2547–2555, doi:10.1557/jmr.2014.287.

[19] A. Jiang, X. Wang, Dendritic and seaweed growth of proeutectic scandium trialuminide in hypereutectic Al-Sc undercooled melt, Acta Mater 200 (2020) 56–65, doi:10.1016/j.actamat.2020.08.078.

[20] A.J. McLeod, L.M. Hogan, C.M. Adam, D.C. Jenkinson, Growth mode of the aluminum phase in Al-Si and Al-Al3Fe eutectics, J. Cryst. Growth. 19 (1973) 301–309, doi:10.1016/0022-0248(73)90054-7.

[21] X. Yang, K. Fujiwara, K. Maeda, J. Nozawa, H. Koizumi, S. Uda, Dependence of Si faceted dendrite growth velocity on undercooling, Appl. Phys. Lett. 98 (2011) 1–4, doi:10.1063/1.3543623.

[22] A. Hellawell, The growth and structure of eutectics with silicon and germanium, Prog. Mater. Sci. 15 (1970) 3–78, doi:10.1016/0079-6425(70)90001-0.

[23] R. Bonnet, M. Loubradou, Crystalline defects in a B.C.T. Al2Cu(θ) single crystal obtained by unidirectional solidification along [001], Phys. Status Solidi Appl. Res. 194 (2002) 173–191 https://doi.org/10.1002/1521-396X(200211)194:1<173::AID-PSSA173>3.0.CO;2-P.

[24] K. Gao, S. Li, L. Xu, H. Fu, Effect of sample size on intermetallic Al2Cu microstructure and orientation evolution during directional solidification, J. Cryst. Growth. 394 (2014) 89–96, doi:10.1016/j.jcrysgro.2014.02.023.

[25] X. Li, Y. Fautrelle, Z. Ren, R. Moreau, Formation mechanism of axial macrosegregation of primary phases induced by a static magnetic field during directional solidification, Sci. Rep. 7 (2017) 1–13, doi:10.1038/srep45834.

[26] K. Gao, Y. Xu, W. Song, L. Guan, M. Li, K. Li, X. Guo, R. Zhang, Preparation and growth characterization of Al2Cu phase crystal with the single orientation under directional solidification, Mater. Res. 21 (2018), doi:10.1590/1980-5373-MR-2018-0381.

[27] Z. Ding, Q. Hu, F. Yang, L. Yu, T. Yang, N. Zhang, W. Lu, Unveiling the Growth Mechanism of Faceted Primary - Al2Cu with Complex Morphologies During Solidification, Acta Metall. Sin. (English Lett. (2021), doi:10.1007/s40195-021-01327-w.

[28] R. Hamar, C. Lemaignan, Facetting behaviour of Al2Cu during solidification, J. Cryst. Growth. 53 (1981) 586–590, doi:10.1016/0022-0248(81)90143-3.

[29] P. Gillon, Uses of intense d.c. magnetic fields in materials processing, Mater. Sci. Eng. A. 287 (2000) 146–152, doi:10.1016/s0921-5093(00)00767-x.

[30] J. Wang, S. Yue, Y. Fautrelle, P.D. Lee, X. Li, Y. Zhong, Z. Ren, Refinement and growth enhancement of Al2Cu phase during magnetic field assisting directional solidification of hypereutectic Al-Cu alloy, Sci. Rep. 6 (2016) 1–6, doi:10.1038/srep24585.

[31] A. Kao, B. Cai, P.D. Lee, K. Pericleous, The effects of Thermoelectric Magneto-hydrodynamics in directional solidification under a transverse magnetic field, J. Cryst. Growth. 457 (2017) 270–274, doi:10.1016/j.jcrysgro.2016.07.003.

[32] J.A. Shercliff, Thermoelectric magnetohydrodynamics in closed containers, Phys. Fluids. 22 (1979) 635–640, doi:10.1063/1.862646.

[33] P. Lehmann, R. Moreau, D. Camel, R. Bolcato, Modification of interdendritic convection in directional solidification by a uniform magnetic field, Acta Mater 46 (1998) 4067–4079, doi:10.1016/S1359-6454(98)00064-0.

[34] Z. Yan, X. Li, Z. Cao, X. Zhang, T. Li, Grain refinement of horizontal continuous casting of the CuNi10Fe1Mn alloy hollow billets by rotating magnetic field (RMF), Mater. Lett. 62 (2008) 4389–4392, doi:10.1016/j.matlet.2008.07.010.

[35] B. Cai, A. Kao, E. Boller, O.V. Magdysyuk, R.C. Atwood, N.T. Vo, K. Pericleous, P.D. Lee, Revealing the mechanisms by which magneto-hydrodynamics disrupts solidification microstructures, Acta Mater 196 (2020) 200–209, doi:10.1016/j.actamat.2020.06.041.

[36] X. Li, Z. Ren, Y. Fautrelle, Effect of a high axial magnetic field on the microstructure in a directionally solidified Al-Al2Cu eutectic alloy, Acta Mater 54 (2006) 5349–5360, doi:10.1016/j.actamat.2006.06.051.

[37] R. Daudin, S. Terzi, P. Lhuissier, J. Tamayo, M. Scheel, N.H. Babu, D.G. Eskin, L. Salvo, Particle-induced morphological modification of Al alloy equiaxed dendrites revealed by sub-second in situ microtomography, Acta Mater 125 (2017) 303–310, doi:10.1016/j.actamat.2016.12.005.

[38] J.L. Fife, J.W. Gibbs, E.B. Gulsoy, C.L. Park, K. Thornton, P.W. Voorhees, The dynamics of interfaces during coarsening in solid-liquid systems, Acta Mater 70 (2014) 66–78, doi:10.1016/j.actamat.2014.01.024.

[39] A.J. Shahani, E.B. Gulsoy, V.J. Roussochatzakis, J.W. Gibbs, J.L. Fife, P.W. Voorhees, The dynamics of coarsening in highly anisotropic systems: Si particles in Al-Si liquids, Acta Mater 97 (2015) 325–337, doi:10.1016/j.actamat.2015.06.064.

[40] M. Drakopoulos, T. Connolley, C. Reinhard, R. Atwood, O. Magdysyuk, N. Vo, M. Hart, L. Connor, B. Humphreys, G. Howell, S. Davies, T. Hill, G. Wilkin, U. Pedersen, A. Foster, N. De Maio, M. Basham, F. Yuan, K. Wanelik, I12: The Joint Engineering, Environment and Processing (JEEP) beamline at Diamond Light Source, J. Synchrotron Radiat. 22 (2015) 828–838, doi:10.1107/S1600577515003513.

[41] N. Wadeson, M. Basham, Savu: A Python-based, MPI Framework for Simultaneous Processing of Multiple, N-dimensional, Large Tomography Datasets, 2016 http://arxiv.org/abs/1610.08015.

[42] Nobuyuki Otsu, A Threshold Selection Method from Gray-Level Histograms, IEEE Trans. Syst. Man Cybern. 9 (1979) 62–66.

[43] M.A. Tschopp, J.D. Miller, A.L. Oppedal, K.N. Solanki, Characterizing the local primary dendrite arm spacing in directionally solidified dendritic microstructures, Metall. Mater. Trans. A Phys. Metall. Mater. Sci. 45 (2014) 426–437, doi:10.1007/s11661-013-1985-3.

[44] F.P. Vidal, J.M. Létang, G. Peix, P. Cloetens, Investigation of artefact sources in synchrotron microtomography via virtual X-ray imaging, Nucl. Instruments Methods Phys. Res. Sect. B Beam Interact. with Mater. Atoms. 234 (2005) 333–348, doi:10.1016/j.nimb.2005.02.003.

[45] H.Z. Wang, D.Y.C. Leung, M.K.H. Leung, M. Ni, A review on hydrogen production using aluminum and aluminum alloys, Renew. Sustain. Energy Rev. 13 (2009) 845–853, doi:10.1016/j.rser.2008.02.009.

[46] K. Gao, S. Song, S. Li, H. Fu, Characterization of microstructures and growth orientation deviating of Al2Cu phase dendrite at different directional solidification rates, J. Alloys Compd. 660 (2016) 73–79, doi:10.1016/j.jallcom.2015.11.093.

[47] H.J. Scheel, Accelerated crucible rotation: a novel stirring technique in high-temperature solution growth, J. Cryst. Growth. (1972) 560–565 13/14.

[48] W. Kurz, C. Bezençon, M. Gäumann, Columnar to equiaxed transition in solidification processing, Sci. Technol. Adv. Mater. 2 (2001) 185–191, doi:10.1016/S1468-6996(01)00047-X.

[49] J. Warren, Rule of thumb breaks down, Nat. Mater. 5 (2006) 595–596, doi:10.1038/nmat1702.

[50] A. Baldan, Progress in Ostwald ripening theories and their applications in nickel-base super alloys, J. Mater. Sci. 37 (2002) 2171–2202.

[51] K.A. Jackson, The interface kinetics of crystal growth processes, Interface Sci 10 (2002) 159–169.

[52] K.A. Jackson, Current concepts in crystal growth from the melt, Prog. Solid State Chem. 4 (1967), doi:10.1016/0079-6786(67)90005-2.

[53] V.K. Ivanov, P.P. Fedorov, A.Y. Baranchikov, V.V Osiko, Oriented attachment of particles: 100 years of investigations of non-classical crystal growth, Russ. Chem. Rev. 1204 (2014) 127–131, doi:10.1016/b978-0-08-012210-6.50078-8.

[54] J.J. De Yoreo, P.U.P.A. Gilbert, N.A.J.M. Sommerdijk, R.L. Penn, S. Whitelam, D. Joester, H. Zhang, J.D. Rimer, A. Navrotsky, J.F. Banfield, A.F. Wallace, F.M. Michel, F.C. Meldrum, H. Cölfen, P.M. Dove, Crystallization by particle attachment in synthetic, biogenic, and geologic environments, Science 80 (2015) aaa6760 349, doi:10.1126/science.aaa6760.

[55] H. Zhang, J.F. Banfield, Energy calculations predict nanoparticle attachment orientations and asymmetric crystal formation, J. Phys. Chem. Lett. 3 (2012) 2882–2886, doi:10.1021/jz301161j.
[56] Y. Grin, F.R. Wagner, M. Armbrüster, M. Kohout, A. Leithe-Jasper, U. Schwarz, U. Wedig, H. Georg von Schnering, CuAl2 revisited: Composition, crystal structure, chemical bonding, compressibility and Raman spectroscopy, J. Solid State Chem. 179 (2006) 1707–1719, doi:10.1016/j.jssc.2006.03.006.
[57] M.H. Nielsen, S. Aloni, J.J. De Yoreo, In situ TEM imaging of CaCO3 nucleation reveals coexistence of direct and indirect pathways, Science 345 (80) (2014) 1158–1162, doi:10.1126/science.1254051.
[58] D.L. Miao Song, Gang Zhou, Ning Lu, Jaewon Lee1, Elias Nakouzi1, Hao Wang, Oriented attachment induces fivefold twins by forming and decomposing high-energy grain boundaries, Science 367 (80) (2020) 40–45, doi:10.1017/cbo9781316389508.016.
[59] X. Li, J. Wang, L. Hou, A. Gagnoud, Y. Fautrelle, Studying on the morphology of primary phase by 3D-CT technology and controlling eutectic growth by tailoring the primary phase, J. Alloys Compd. 821 (2020), doi:10.1016/j.jallcom.2019.153457.
[60] W. Kurz, D.J. Fisher, Fundamentals of Solidification, 4th rev. e, 1992.